Published in final edited form as:
Nature. 2020 December 01; 588(7838): 498–502. doi:10.1038/s41586-020-2665-2.

Structures and distributions of SARS-CoV-2 spike proteins on intact virions

Zunlong Ke[#1], **Joaquin Oton**[#1], **Kun Qu**[#1], **Mirko Cortese**[2], **Vojtech Zila**[3], **Lesley McKeane**[4], **Takanori Nakane**[1], **Jasenko Zivanov**[1], **Christopher J. Neufeldt**[2], **Berati Cerikan**[2], **John M. Lu**[1], **Julia Peukes**[1], **Xiaoli Xiong**[1], **Hans-Georg Kräusslich**[3,5], **Sjors H.W. Scheres**[1], **Ralf Bartenschlager**[2,5], **John A.G. Briggs**[1,*]

[1]Structural Studies Division, Medical Research Council Laboratory of Molecular Biology, Cambridge CB2 0QH, United Kingdom

[2]Department of Infectious Diseases, Molecular Virology, Heidelberg University, 69120 Heidelberg, Germany

[3]Department of Infectious Diseases, Virology, Heidelberg University, 69120 Heidelberg, Germany

[4]Visual Aids Department, Medical Research Council Laboratory of Molecular Biology, Cambridge CB2 0QH, United Kingdom

[5]German Center for Infection Research, Heidelberg partner site, 69120 Heidelberg, Germany

[#] These authors contributed equally to this work.

Abstract

Severe acute respiratory syndrome coronavirus 2 (SARS-CoV-2) virions are surrounded by a lipid bilayer from which spike (S) protein trimers protrude[1]. Heavily glycosylated S trimers bind the ACE2 receptor and mediate entry of virions into target cells[2–6]. S exhibits extensive conformational flexibility: it modulates exposure of its receptor binding site and later undergoes complete structural rearrangement to drive fusion of viral and cellular membranes[2,7,8]. The structures and conformations of soluble, overexpressed, purified S proteins have been studied in detail using cryo-electron microscopy[2,7,9–12]. The structure and distribution of S on the virion surface, however, has not been characterised. Here we applied cryo-electron microscopy and tomography to image intact SARS-CoV-2 virions, determining the high-resolution structure, conformational flexibility and distribution of S trimers *in situ* on the virion surface. These results reveal the conformations of S present on the virion, and provide a basis from which to understand interactions between S and neutralizing antibodies during infection or vaccination.

---

[*] correspondence to JAGB: jbriggs@mrc-lmb.cam.ac.uk.

Author contributions
ZK and JAGB conceived the study, ZK, JO, KQ, MC, VZ, HGK, RB and JAGB designed the study. MC, VZ, CJN and BC prepared and characterized virus samples with supervision from HGK and RB. ZK and KQ collected cryo-EM data. ZK, JO and KQ processed cryo-EM data with assistance from TN, JZ, JML and JP, supervised by SHWS and JAGB. ZK, JO, KQ, MC and LM made figures. ZK, JO, KQ, MC, XX and JAGB interpreted data. JAGB prepared the initial draft and managed the project. ZK, JO, KQ, MC and JAGB wrote the manuscript with input from all authors. SHWS, HGK, RB and JAGB obtained funding.

Competing interests: The authors have no competing interests.

Severe acute respiratory syndrome coronavirus 2 (SARS-CoV-2) is a betacoronavirus[13,14], an enveloped virus containing a large nucleoprotein (N)-encapsidated positive sense RNA genome[15]. Three transmembrane proteins are incorporated into the viral lipid envelope: spike protein (S) and two smaller proteins, membrane protein (M) and envelope protein (E)[1,15]. When imaged by cryo-electron microscopy (cryo-EM), betacoronaviruses appear as approximately spherical particles, with variable diameters centered around 100 nm, containing a dense viroplasm, and bounded by a lipid bilayer from which prominent S trimers protrude[16,17]. S trimers of SARS-CoV-2 bind to the receptor, ACE2, on the surface of target cells and mediate subsequent viral uptake and fusion[2–5,7]. In doing so S undergoes a dramatic structural rearrangement from the prefusion form to the postfusion form[8]. The overall architectures of both pre and postfusion forms are well conserved among coronaviruses[8,18,19].

During infection, coronaviruses extensively remodel the internal membrane organisation of the cell, generating viral replication organelles in which replication takes place[20–22]. The S protein, together with the other membrane protein M, and E, are inserted into membranes of the endoplasmic reticulum (ER), and traffic to the ER Golgi intermediate compartment (ERGIC). The encapsidated genome buds into the ERGIC to form virions which are then trafficked to the plasma membrane and released[20–22]. S is primed for membrane fusion by proteolytic cleavage at the S1/S2 site, and subsequently the S2’ site[23].

The prefusion structure of S from coronaviruses including SARS-CoV-2 has been extensively studied using ectopic expression of soluble, secreted forms of S, followed by purification and cryo-EM[2,7,9–11]. In the prefusion form, the receptor binding domain (RBD) sits at the top of a broad, trimeric spike, above the fusion core. Three copies of the RBD are surrounded by three copies of the N-terminal domain (NTD) which show some mobility[2,7–9]. In the closed prefusion conformation all three copies of the RBD lay flat on the spike surface, largely occluding the receptor binding site, while in the open prefusion conformation one or multiple RBDs lift up to expose the receptor binding site[2,7,9,10]. The surface of the trimer is extensively glycosylated with 22 potential N-linked glycosylation sites per monomer[2,6,7]. After receptor binding, structural transition of the prefusion to the postfusion form brings the fusion peptide and the transmembrane domain together at one end of a long, needle-like structure centered around a three-helix bundle[8]. Five N-linked glycans are spaced along the length of the postfusion spike[8].

Fully understanding how S proteins function and how they interact with the immune system, requires knowledge of the structures, conformations and distributions of S trimers within virions. Here we have applied cryo-EM methods to study the structure, conformations and distributions of S trimers *in situ* on the virion surface.

To avoid artefacts associated with virus concentration or purification, we aimed to image SARS-CoV-2 virions from the supernatant of infected cells without virus concentration or purification. VeroE6 cells were infected with SARS-CoV-2 (isolate Germany/BavPat1/2020)[24]. At 48 h post-infection, supernatant was clarified, inactivated by fixation with formaldehyde and stored at -80 °C. Western blot revealed that approximately 45% of total S protein monomers on virions has been cleaved at the multibasic cleavage site into S1 and S2 (Fig. 1a). Fixed supernatant was vitrified by plunge freezing and imaged by cryo-EM. Fixation may help to stabilize some protein conformations by crosslinking, but is not expected to give rise to any new conformations. As expected, given the concentration of virus in cellular supernatants (around 10^7 plaque forming units/ml), small numbers of individual virions were found scattered around the grid – these were imaged by cryo-electron tomography (cryo-ET) (Fig. 1b).

Virions were approximately spherical with a diameter to the outside of the lipid bilayer of 91 ± 11 nm (n=179) (Extended Data Fig. 1a). They contain granular densities corresponding to N, and are studded with S trimers (Fig. 1b,c). These features are generally consistent with those of other coronaviruses imaged by cryo-EM[1,16,17]. S trimers protruding from the viral surface had two morphologies – a minority were extended thin structures reminiscent of the postfusion form, while the majority are wider structures reminiscent of the prefusion form. This observation contrasts with a recent preprint showing cryo-EM images of purified SARS-CoV-2 virions inactivated with the nucleic acid modifier β-propiolactone in which only thin protrusions were seen on the viral surface[25], and is consistent with *in situ* observations of virus assembly[21].

We also collected tomograms of SARS-CoV-2 virions produced by infection of Calu-3 cells, a human lung carcinoma cell line that supports virus production to a titre comparable to Vero cells. The morphology of the virions and the appearance of the S trimers on the surface was consistent with that seen for virions produced from VeroE6 cells (Extended Data Fig. 2a-c). Western blot analysis showed that approximately 73% of S was in the cleaved form (Extended Data Fig. 2d).

Individual virions contained 24 ± 9 S trimers (Extended Data Fig. 1b). This value is lower than previously estimated assuming an equidistant distribution of S[21], because S is not uniformly distributed over the virus surface. A small sub-population of virions contained only few S trimers while larger virions contained more S trimers (Extended Data Fig. 1b). We identified 4,104 wide S trimers and 116 thin S trimers from 179 virions and subjected them to subtomogram averaging. The averaged structures, at 7.7 and 22 Å resolution, respectively, correspond very well to published structures of purified S trimers in the pre- and postfusion forms[2,7,8] (Fig. 2a). Overall, approximately 97% of S trimers are in the prefusion form, and 3% in the postfusion form. Pre- and postfusion forms appear to be distributed evenly among virions.

Prefusion S trimers on the virus surface may be predominantly closed, with the open conformation induced or stabilized by ACE2 binding, or the open form may also be present. Open or closed forms may induce different ranges of antibodies when used as immunogens and there are ongoing efforts to generate S protein constructs stabilized in one or other conformation[9,11,12]. To assess whether S trimers are present in open and/or closed conformations, we subjected the RBD regions of individual monomers within the trimers to classification. Three kinds of classes were found, those with the RBD in the closed position, those with the RBD in the open position, and those where the RBD was predominantly in the closed position, but with some weakening of the density, suggesting the presence of more mobile conformations (Extended Data Fig. 3). Considering the classes to which each monomer was assigned, we derived structures of fully closed trimers, and of trimers where one RBD is open, which represent ~31% and ~55% of 3,854 prefusion trimers) (Fig. 2b, Extended Data Fig. 4). We also identified a small number of trimers (~14% of 3,854 prefusion trimers) in which two RBDs are in the open conformation (Fig. 2b). These observations confirm that the opening of the RBD observed in recombinant S trimers also takes place on the virus surface, and that artificial S protein constructs stabilized in the closed and open conformations both represent structures present *in situ*. The receptor binding site is therefore stochastically exposed *in situ*, and available to interact with ACE2 and with antibodies.

The trimers do not all protrude straight from the viral surface. They can tilt by up to 90° towards the membrane, though tilts over 50° are decreasingly favoured (Extended Data Fig. 1c,d). We grouped trimers according to their orientation relative to the membrane, and averaged these groups independently. The averaged structures reveal that the membrane-proximal stalk region acts as a hinge with sufficient flexibility to allow tilting in all directions (Fig. 2c).

We generated models of individual virus particles, with S trimers located at the position, orientation and conformation that were determined by subtomogram averaging (Fig. 2d). S trimers appear to be distributed randomly on the viral surface, with no obvious clustering or relationship between location, orientation, and conformation. There is approximately one trimer per 1,000 nm^2 of membrane surface compared to approximately one per 100 nm^2 for influenza A virus[26]. The sparse distribution of S, together with the predominantly closed state, suggest that receptor binding may be less dependent on avidity effects than is the case for pandemic influenza viruses[27]. This is consistent with the higher affinity between S and ACE2 (in the nM range[2,7]) than between haemaglutinin and sialic acid (mM range[27]).

The low concentration of particles in supernatant makes high-resolution structure determination difficult. We therefore concentrated the virus by pelleting through a sucrose cushion. Concentrated virions deviate from spherical morphology (Extended Data Fig. 5), but overall features are preserved. We performed cryo-ET and subtomogram averaging on the particles, and saw predominantly prefusion S trimers, with occasional postfusion S trimers. Upon classification of the prefusion S we were only able to identify the RBD in the closed position, and monomers in which a weak RBD density is observed (Extended Data Fig. 3c).

Virions in the supernatant from infected cells show primarily prefusion S trimers which are in either closed or open prefusion conformations. Virions concentrated through a sucrose cushion continue to show prefusion conformations, but the open conformation is no longer observed. Other studies have shown that virions inactivated with β-propiolactone, rather than formaldehyde, are primarily in a postfusion state[25]. S trimers purified from membranes are found only in the closed prefusion and postfusion conformations[8], while other studies have suggested that the open RBD in soluble S trimers is found in a continuum of different positions[28]. These observations suggest that the open prefusion conformations of the spike protein we observe before, but not after concentration, are fragile (despite the fixation applied here) and may be affected by purification procedures.

Our data imply that inactivation and purification methods can alter the ratio of pre and postfusion forms, and the ratio of open and closed forms. It has been speculated that substantial amounts of postfusion S on the virus surface may protect the virus by shielding the prefusion form or may shift the host response towards non-neutralizing antibodies[8]. Given the small fraction of postfusion spikes we observed on intact virions we consider it unlikely that this is an important defence mechanism for the virus during infection, but it may be an important consideration for vaccination. Candidate vaccines based on inactivated virus particles are under development. These may present different S protein epitopes to the immune system depending on how they are prepared and therefore differ in their ability to induce a neutralizing response. For example, β-propiolactone is frequently used in vaccine production (such as for influenza virus subunit vaccines[29]), but if postfusion S induces non-neutralizing responses, β-propiolactone may not be optimal for inactivation during SARS-CoV-2 S vaccine formulation.

We next imaged the concentrated virus in 2D by cryo-EM and performed single-particle analysis on those prefusion S trimers that protruded from the sides of the virus particles, generating a consensus structure of the prefusion trimer at 3.4 Å resolution. Focussed classification with partial signal subtraction on individual RBD monomers led to two classes (Extended Data Fig. 5). Consistent with the absence of open conformations in this sample by cryo-ET, we observed 81% of the monomers in which the RBD is in the closed conformation and 19% of the monomers in which density for the RBD is weaker, but predominantly in the closed position. We refined the structures of S trimers in which all three RBDs are in the closed conformation (53% of the data), and those in which at least one RBD is weak (47% of the data), to resolutions of 3.5 Å and 4.1 Å, respectively (Fig. 3a, Extended Data Fig. 6). The two structures are highly similar, differing only in the density levels for one RBD. We used the structure with three closed RBDs to build and refine an atomic model of the S protein trimer *in situ* on the viral surface.

The positions of glycans on the surface of S are well resolved in our structure with density at 17 of the 22 predicted N-glycosylation sites (Fig. 3b). The other 5 glycosylation sites are in disordered NTD loops or in the stalk region and are not resolved at high resolution. At the base of the trimer a clear ring of glycans forms a collar above the stalk region. The density for the stalk region extends by 2 helical turns compared to published structures of soluble ectodomain and further at lower resolution before fading out due to stalk flexibility (Fig. 3c). SARS-CoV-2 S trimers are sparsely distributed and can be highly tilted towards the membrane. This implies that epitopes at the base of the head domain and in the stalk region, would be accessible to antibodies where they are not protected by the extensive glycan shell.

We compared the *in situ* structure of the S trimer to structures previously obtained using exogenously expressed purified protein. A recent study of full-length trimeric S solubilized in detergent micelles[8], identified two features that are not seen in most structures of soluble S ectodomain trimers: well-defined density for residues 14-26 of S; and a folded loop between residues 833 and 853. This loop is folded in the structure of the “locked” conformation of the ectodomain[9], and may become folded in the low-pH conditions in the endosome[30]. We observe only weak density for residues 14-26, and we do not observe folded structure for the 833-853 region. The SARS-CoV-2 strain we have imaged contains the widely circulating D614G substitution[31], this mutation abolishes a salt bridge to K854 (Fig. 3d) and may reduce folding of the 833-854 loop[9,30]. We did not observe additional density that would correspond to bound lipids such as those described in a recent preprint[10], or other bound co-factors. These may be present sub-stoichiometrically or in rare conformations but are not a general feature of the S trimer *in situ*. Overall, our structure is very similar to that of the soluble trimeric ectodomain in the closed prefusion form stabilized by a double proline mutation (Extended Data Fig. 7)[2,7]. This provides an important validation of the ongoing use of recombinant, purified S trimers for research, diagnostics and vaccination – they indeed represent the *in situ* structure of S. By demonstrating structure determination of S trimers to 3.4 Å resolution on the virion surface (Fig. 3), our data make us optimistic that cryo-EM can be used to study antibody binding to S in the context of the viral surface. Such studies could provide insights into how neutralizing antibodies block virus infection, particularly for antibodies against membrane-proximal regions of S, and thus can inform design of immunogens for vaccination.

Materials and methods

Cells and Virus

VeroE6 cells were obtained from ATCC and were cultured in Dulbecco’s modified Eagle medium (DMEM, Life Technologies) containing 10% fetal bovine serum, 100 U/mL penicillin, 100 μg/mL streptomycin and 1% non-essential amino acids (complete medium). The Germany/BavPat1/2020 SARS-CoV-2 was isolated by Prof. Christian Drosten, Charité, Berlin, and distributed by the European Virology Archive (Ref-SKU: 026V-03883) at passage 2 (P2). A stock of SARS-CoV-2 was obtained by passaging the virus once in VeroE6 cells (P3). To produce SARS-CoV-2 virions, VeroE6 cells grown on 75 cm^2 side-bottom tissue culture flasks were infected with SARS-CoV-2 (P3) at MOI of 0.5. Culture media from infected cells were harvested at 48 h postinfection, clarified by centrifugation at 1,000 × g for 10 min, cleared through a 0.45-μm nitrocellulose filter and fixed with 4% formaldehyde for 30 min at RT. Culture medium was supplemented with 10 mM HEPES (pH 7.2) prior to fixation. Virus-containing medium was subsequently aliquoted and stored at −80 °C. Infectious supernatants containing SARS-CoV-2 virions were obtained from Calu-3 cells infected with P3 virus at an MOI = 5 for 48 h and processed as described above.

To obtain SARS-CoV-2 virions at high concentration, infection and harvest of VeroE6 culture medium were performed as above, followed by concentration of fixation-inactivated virions from media by ultracentrifugation through a 20% (wt/wt) sucrose cushion (120 min at 27,000 rpm in a Beckman SW32 rotor; Beckman Coulter Life Sciences). Pelleted particles were resuspended in PBS and stored in aliquots at −80 °C.

Western blot

VeroE6 or Calu-3 cells mock infected or infected for 48 h with SARS-CoV-2 (MOI = 5) were washed twice in PBS, scraped, pelleted at 700 x g for 5min and lysed in PBS pH 7.4, containing 1% Triton-X 100 and protease inhibitors (Merck) for 30 min at 4 °C. Samples were centrifuged at 4 °C for 30 min and supernatants were collected. Total protein concentration was calculated using the Bio-Rad Protein Assay kit (Biorad). Purified viruses were prepared for western blot by centrifugation of 32 ml of virus containing supernatants on a 10% sucrose cushion in a Beckmann J25 centrifuge. Centrifugation was performed at 10,000 x g for 4 h at 4 °C. Supernatants were discarded and purified virus pellet were resuspended in 500 µl of PBS. For western blotting, 10 µg of total cell lysates and 5 µl of purified viruses were diluted in Laemmli buffer and loaded on a pre-casted Criterion XT 4-12% gradient gel (Biorad). Gels were transfered to PVDF membrane using a wet-electroblotting chamber system (Biorad) in Towbin buffer containing 10% methanol. Transfer was performed overnight at 4 °C. Membranes were washed in PBS and blocked with 10% milk in PBS containing 0.2% tween-20 (PBS-T) for 1 h. Membranes were incubated for 1 h at RT with primary antibodies specific for an epitope in the C-terminal region of S (Abcam, cat# ab252690, diluted 1:1,000 in PBS-T), for N-protein (Sino Biological, cat# 40143-MM05, diluted 1:1,000 in PBS-T), or non-structural protein 3 (nsp3) (abcam, cat# ab181620, diluted 1:500 in PBS-T). Next, the membranes were washed 3 times in PBS-T, incubated with HRP conjugated anti-mouse or anti-rabbit antibodies at 1:10,000 dilution for 1 h, washed again 3 times in PBS-T, incubated with western Lightning Plus-ECL reagent (Perkin Elmer; Waltham, MA) and imaged using an Intas ChemoCam Imager 3.2 (Intas, Göttingen). Densitometric analysis of western blot assays was performed using LabImage 1D L340 software version 4.1 (Intas, Göttingen). The blot shown is representative of three independent experiments. Uncropped, unprocessed blots are in the Source Data file.

RT-PCR and spike sequencing

Total RNA was isolated from infected VeroE6 cells 48 h after infection with Germany/BavPat1/2020 SARS-CoV-2 (P2). Spike cDNA was produced from the total RNA using superscript iii (ThermoFisher) with specific RT-primers (CAATTGTGAAGATTCTCATA). The cDNA was amplified by PCR using specific primers (Fwrd – ATGTTTGTTTTTCTTGTTTTATT; rev – TTATGTGTAATGTAATTTGA) and the resulting amplicon was sent for Sanger sequencing. Sequences were compared to the Germany/BatPat1/2020 SARS-CoV-2 reference sequence (Ref-SKU: 026V-03883) and found to be identical. Specific sequencing primers: Fwrd1 - ATGTTTGTTTTTCTTGTTTTATT; Fwrd2 – GGTTGGACAGCTGGTGCT; Fwrd3 – CCAACCATACAGAGTAGTAGTA; Rev1 – GTAGCAGCAAGATTAGCAGAA; Rev2 – TTATGTGTAATGTAATTTGA.

Cryo-ET sample preparation

Fixed virus samples from the supernatant of infected cells without any concentration step (unconc) or concentrated by pelleting through a sucrose cushion (conc) were prepared, imaged, and processed in parallel. The virus suspension was mixed with 10-nm colloidal gold (in PBS solution) in 10:1 ratio. Then 3 µl of the solution was added to a glow-discharged copper grid (C-Flat 2/2, Protochips). Grids were plunge frozen into liquid ethane by back-side blotting using a LeicaGP cryo plunger (Leica) and stored in liquid nitrogen until imaging.

Cryo-ET data collection

Cryo-ET data collection was performed essentially as described previously[32]. Cryo-grids were loaded into an FEI Titan Krios transmission electron microscope operated at 300 kV and images were recorded on a Gatan K2 Summit direct detection camera in counting mode with a 20 eV energy slit in zero-loss mode. Tomographic tilt series between −60° and +60° were collected using SerialEM 3.8.0 software[33] in a dose-symmetric scheme[34] with a 3° angular increment. A total dose of 120 e^-/A^2 per tilt series was distributed evenly among 41 tilt images. The nominal magnification was 81,000 X, giving a pixel size of 1.532 Å on the specimen. The defocus range was between -2 µm and -6 µm and 10 frames were saved for each tilt angle. All data acquisition parameters are listed in Extended Data Table 1.

Frames were motion-corrected in IMOD 4.10.30[35] and images were dose-filtered using the *alignframes* function in IMOD. Exposure filtering was implemented according to the cumulative dose per tilt as described elsewhere[36]. The contrast transfer function (CTF) was measured using non-dose-filtered images using the ctfplotter package within IMOD[37]. Tilt series stacks were sorted using IMOD *newstack* function and fiducial-alignment of all tilt series was performed in IMOD/etomo. Tomograms with less than three trackable gold fiducials were discarded. Motion-corrected and dose-filtered tilt stacks were CTF-corrected by CTF multiplication and tomograms were reconstructed by weighted back-projected in novaCTF[38]. Tomograms were low-pass filtered to 50 Å for better visualization in EMAN2.2[39] and tomographic slices were visualized with IMOD.

Extraction of S trimers from tomograms

The initial steps of subtomogram alignment and averaging were implemented using MATLAB (MathWorks) scripts which were derived from the TOM[40] and AV3[41] packages as described previously[32]. The missing wedge was modelled as the summed amplitude spectrum of background subtomograms for each tomogram, and was applied during alignment and averaging.

To generate an initial template model of the spike protein from the viral surface, 68 spikes were manually picked from four virions of tomograms that were down-scaled by 4x binning of the voxels. The 68 spikes' initial Euler angles (2 out of 3) were determined based on the vector between two points, one on the head of the spike and one on the membrane where the spike anchors, respectively. The 68 spikes were iteratively aligned to one another for four iterations applying three-fold symmetry to generate a low-resolution template that resembled a prefusion conformation of the spike. This template was used as an alignment reference for all virions (below). All postfusion spikes were manually identified and picked and initial Euler angles were assigned in the same manner.

The center of each virion was then marked manually using the Volume Tracer function in UCSF Chimera (version 1.13.1)[42] and the radius of the virion was determined centered at the membrane using the Pick Particle Chimera Plugin[43]. An oversampled spherical grid of points was generated on the virion surface with ~9 nm spacing, and subtomograms were extracted for all grid points with a box size of 96 pixels (approximately 60 nm) centered at a radius 14 nm above these grid positions (approximately the radius of the expected center of the spike). Initial Euler angles were assigned to each subtomogram based on the orientation of the normal vectors relative to the sphere surface.

Subtomograms were aligned against the low resolution template (from the above average of 68 spikes). During this alignment, subtomogram positions converged onto clusters at the true spike positions. One subtomogram position was kept for each cluster, excluding particles within a distance of ~15 Å (10 pixels) and removing particles with cross-correlation coefficients (CCC) below 0.11. Subtomograms that had tilted by more than 90° relative to their perpendicular positions were excluded. Visual inspection of the tomograms using the Place Object Chimera Plugin[43] confirmed that subtomograms selected in this manner corresponded to S trimers on the viral surface (see below). Subtomograms were divided into two halves based on virion number. From this point on the two halves were processed independently.

Subtomogram averaging

Subsequent processing was performed in RELION[44]. For this purpose, subtomograms were reconstructed from the original tilt series images after motion correction using *relion_reconstruct*. Using dedicated python scripts, the S trimer positions in the 3D tomograms from the procedure outlined above were converted into 2D positions and defocus values in the corresponding tilt series images, as well as Euler angles in the RELION convention. Individual sub-tomograms were reconstructed at a 2x down-scaled pixel size of 3.064 Å, by 3D insertion of Fourier slices of the cropped regions of the tilt series images, each multiplied by their corresponding CTF, which included the dose filter. Similarly, 3D-CTF volumes were generated by 3D insertion of the corresponding CTF^2 slices. Subtomograms were reconstructed in a box size of 128 voxels for prefusion trimers and a box size of 192 voxels for averages of tilted spikes and for postfusion trimers.

In order to deal with the CTF pre-multiplied sub-tomograms, as well as the multiplicity of each 3D voxel in the tilt series, a modified version of RELION was used for subtomogram refinement and classification (details to be described elsewhere). Standard 3D auto-refinement was performed with C3 symmetry and a soft-edged mask around the trimers, using a 30 Å low-pass filtered map as an initial reference. Using 3,854 of the 4,104 subtomograms (excluding those that had tilted by more than 90° relative to the perpendicular position (Extended Data Fig. 1c)), a 7.7 Å consensus map was calculated for the prefusion trimers; 116 postfusion trimers led to a 22 Å map.

Angular density (Extended Data Fig. 1c) was illustrated by dividing the number of spikes per histogram bin by the sine of the tilt angle. From this histogram, the noise level in the distribution due to incorrectly aligned spikes was estimated assuming they are uniformly distributed (red dashed line in Extended Data Fig.1c), and based on averaging over the range 140-180°. Such angles must be incorrectly alignments because they orient the spike towards the inside of the virus.

Based on the subtomograms that contributed to the consensus map we estimated that there are 23 ± 9 prefusion S trimers per virion. For a subset of 28 virions, we visually compared the trimers identified by subtomogram averaging with the tomograms to identify false positives or false negatives, finding that the number of S trimers identified by subtomogram averaging is an underestimate of the number of observed S trimers by 0.9 trimers per virion. On this basis we estimate there are 24 ± 9 prefusion S trimers per virion.

Next, we performed symmetry expansion[45], followed by focused classification without alignment and with partial signal subtraction, while keeping the orientations from the consensus refinement fixed. The mask used for focused classification was generated manually and enclosed the RBD of one monomer (Extended Data Fig. 3a), including the closest NTD of the neighbouring monomer. Classification of the primary dataset (unconc1) led to three different RBD states: closed (45% of the monomers); open (28%) and with weak density (27%) (Extended Data Fig. 3a). Classification of a second, smaller data set of virus particles in supernatant (unconc2), comprising 1,224 trimers yielded 39% closed RBD, 22% open RBD and 39% weak RBD, in general agreement with the unconc1 results (Extended Data Fig. 3b). Classification of a dataset of virus particles after concentration through a sucrose cushion (conc), comprising 3,788 trimers, yielded 67% of the monomers corresponding to closed RBDs and 33% to RBDs with weak density. For this data set, no RBDs in the open conformation were identified (Extended Data Fig. 3c).

The classification of the RBDs as closed, open or with weaker density was used to divide the unconc1 dataset into three subsets: 31% (1,175 trimers) have no open RBDs; 55% (2,121 trimers) have one RBD in the open state; and 14% (525 trimers) have two open RBDs. The remaining 33 trimers have three RBDs in the open state and not further processed. In the class with weaker density, the RBD appears to be predominantly in the closed state and was treated as closed for this assignment. For each of the three subsets, reconstruction of the two independently refined half sets was performed using the orientations from the consensus refinement that gave the 7.7 Å consensus map described above. Subsequent standard post-processing procedures for resolution estimation, map sharpening and local-resolution filtering in RELION led to three final maps. The subset with no open RBDs gave a reconstruction with C3 symmetry in which all three RBDs were closed at 8.6 Å resolution. The other two subsets yielded structures with C1 symmetry and either one or two open RBDs, with resolutions of 8.6 Å and 9.9 Å, respectively (Extended Data Figs. 3 and 4). Note, that while fixation is not expected to give rise to any new conformations, we cannot rule out that it differentially stabilizes different conformations, and the position of the equilibrium between open and closed conformations in unfixed samples may differ from those estimated from fixed samples.

Averages of tilted spikes were generated by grouping according to the tilt and rotation of the subtomogram away from the normal vector to the membrane. Subtomograms were included in a group for averaging if they were within 15° of the displayed tilt (0°, 30° and 60°) and rotation (0°, 60°). The pools illustrated in Fig. 2c contain 14.5, 14.1, 12.0 and 10.0% of the subtomograms.

Cryo-EM sample preparation and data collection

Virus solution concentrated through a 20% (wt/wt) sucrose cushion was frozen on C-Flat 2/2 3C grids (Protochips) following the same procedure as for cryo-ET, but without adding gold fiducials. Grids were imaged on a Thermo Fisher Scientific Titan Krios transmission electron microscope that was operated at 300 kV, using a Gatan K3 direct electron detector and a Gatan BioQuantum energy filter with a 20 eV energy slit. Movies with 48 frames and an accumulated dose of 50 $e^-/Å^2$ were acquired in counting mode using SerialEM-3.8.0[33] at a nominal magnification of 81,000 X, corresponding to a calibrated pixel size of 1.061 Å/pixel. Detailed data acquisition parameters are summarized in Extended Data Table 2.

Cryo-EM image processing

The Scheduler functionality in RELION-3.1 was used for fully automated real-time processing during data collection[9,46]. Movies were motion-corrected and dose-weighted using RELION'’s implementation of the MotionCor2 algorithm[47]. Subsequently, non-dose-weighted sums were used to estimate the contrast transfer function (CTF) in CTFFIND-4.1.13[48]. S trimers that were extending from the sides of virus particles were picked manually (973 particles from the first 100 micrographs) and then used as a training set for optimisation of the convolutional neural network in the automated particle picking software Topaz[49]. Extracted particles were subjected to 3D classification using a previously determined structure of the S trimer[9], lowpass-filtered to 30 Å, as initial 3D reference. The selected 286,407 particles that contributed to 3D classes corresponding to S trimers were submitted to Bayesian polishing to correct for per-particle beam-induced motions and a second round of 3D classification to select the 55,159 particles that contributed to the best class. This final consensus set of particles was subjected to CTF refinement of per-particle defocus, per-micrograph astigmatism and beam tilt, followed by a second round of Bayesian polishing. 3D auto-refinements were performed with the selected particles after each round of 3D classification, CTF refinement or Bayesian polishing. The consensus structure had a resolution of 3.4 Å.

Subsequently, symmetry expansion[45], followed by focused 3D classification with partial signal subtraction[50] was performed. Using a mask on a single RBD to focus classification into six classes, while keeping the orientations of the last consensus refinement fixed, resulted in the identification of two RBD states: closed or with weak density. S trimers with all three RBDs in the closed state were refined separately from S trimers with one RBD with weak density, resulting in two final maps with resolutions. Standard RELION post-processing was used for resolution estimation, map sharpening and local-resolution filtering. The C3 symmetric map with three closed RBD had an estimated overall resolution of 3.5 Å; the C1 map with one weaker RBD extended to 4.1 Å resolution (Extended Data Fig. 6b).

Model building and refinement

The SARS-CoV-2 S trimer structure (PDBID: 6ZP0[9]) was used as an initial model for building into the model with three closed RBDs (Extended Data Fig. 6a, middle). Residues were adjusted manually in Coot 0.9[51]. Steric clash and sidechain rotamer conformations were improved using the Namdinator web server[52]. After further iterations of manual adjustment, the structure was refined in PHENIX-1.18.2[53]. The geometry and statistics are given in Extended Data Table 2. The unmasked model-to-map FSC was calculated in PHENIX for the refined model against the full reconstruction.

3D model of spikes on authentic virions

In order to visualize the spike protein on the authentic SARS-CoV-2 virions, the coordinates, orientations and conformational classes determined by subtomogram averaging were converted into a format compatible with Maxon Cinema 4D (version S22.116), and imported together with the 3D models of the different conformational states determined by subtomogram averaging. To generate representative virion images in Fig. 2d we removed the 3 false positives from one virion and positioned the 3 false negatives on each virion which had been identified by visual inspection of the data (see above). The HR2 region was modeled as a cylinder. Images of individual virions from the dataset were rendered into Adobe Photoshop to generate images for presentation.

Extended Data

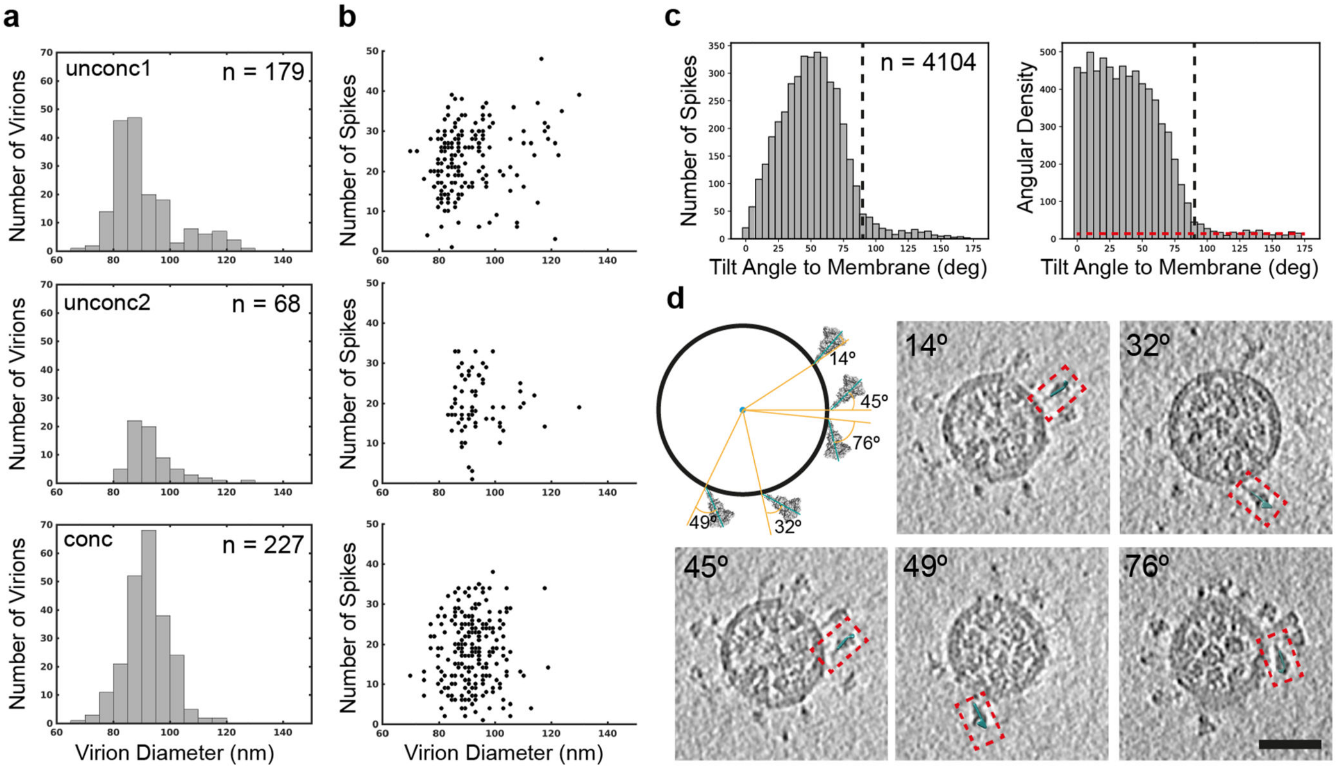

Extended Data Fig. 1. Characterization of SARS-CoV-2 virion morphology.

(**a**) Histogram of virion diameters for unconcentrated extracellular virions in the supernatant of two independent preparations (top and middle), and for extracellular virions after concentration through a sucrose cushion (bottom). After concentration the virions become less spherical. Mean and standard deviation for diameters are 91 ± 11 nm (n=179), 94 ± 9 nm (n=68) and 92 ± 8 nm (n=227) for the three preparations. (**b**) Scatter plot of number of spikes identified per virion during subtomogram averaging against virion diameter for the same virions shown in panel (**a**). Visual inspection indicates that almost all spikes were identified for virions in the supernatant, but that not all spikes are identified in the concentrated preparation leading to an underestimate of the number of spikes. (**c**) Histogram of spike tilt angle towards the membrane for the larger supernatant virus dataset (unconc1). The vertical black dashed line indicates 90°. 97% of particles have tilts below 90°; particles with tilts above 90° were not included in image analysis. The angular density (right) is calculated by dividing the number of spikes by the sine of the determined angle. If spikes were unconstrained in tilt, this distribution would be uniform. The angular density decreases from ~50°, indicating that higher tilts are disfavoured. The horizontal red dashed line indicates the angular distribution of noise (spikes which have failed to align), estimated based on the angular density between 140° and 180°. (**d**) Schematic diagram and examples of individual tilted spikes on virions. The schematic indicates the angle that was measured. Five examples of individual tilted spikes are marked on tomographic slices through an intact virion, with their associated angle. Scale bar 50 nm.

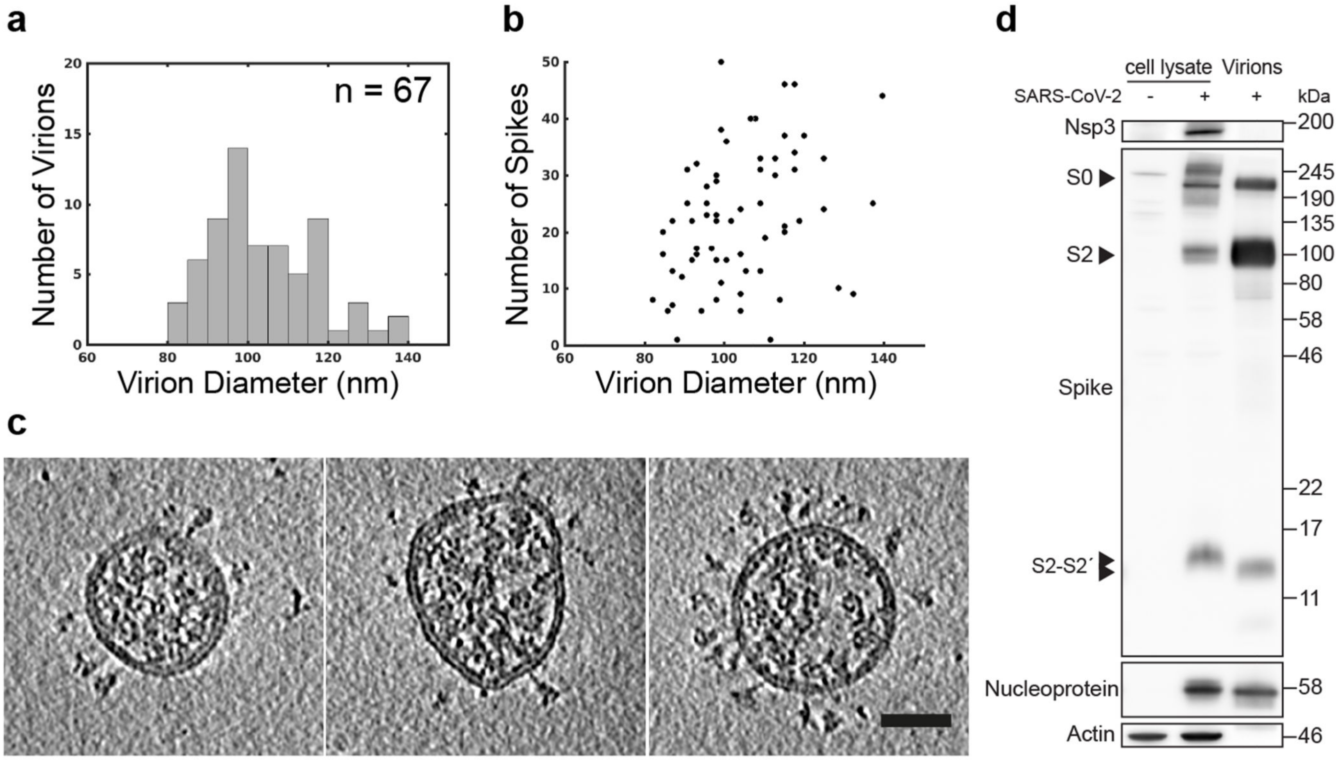

Extended Data Fig. 2. Morphology of SARS-CoV-2 virions released from infected Calu-3 cells.

As in Extended Data Fig. 1, (**a**) Histogram of virion diameters. Mean and standard deviation for diameters are 104 ± 13 nm (n=67). (**b**) Scatter plot of number of spikes identified per virion during subtomogram averaging against virion diameter for the same virions shown in panel a. (**c**) central slices through three representative viruses from 67 imaged in one experiment. Virions from Calu-3 cells had a slightly broader diameter distribution than those from VeroE6 cells. Scale bar 50 nm. (**d**) Western blot analysis of SARS-CoV-2 nsp3, S and N in cell lysates and in virus preparations. In released virions, S is present in both cleaved (S2, 73%) and uncleaved forms (S0, 27%).

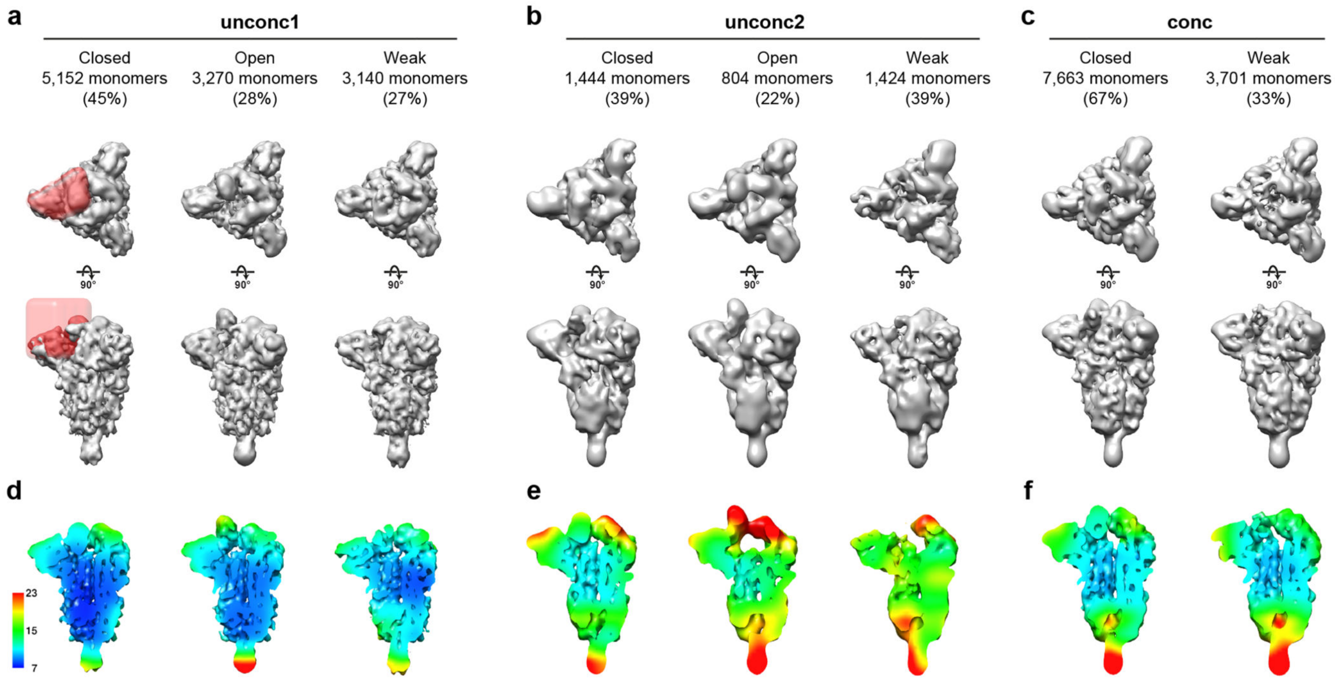

Extended Data Fig. 3. Classification of SARS-CoV-2 spike RBDs.

(**a**) Class averages obtained after focussed classification on the RBD of the left monomer after symmetry expansion of the unconc1 dataset. Top views and side views are shown for closed, open and weak classes. The region subjected to classification is indicated by a transparent red mask surface in the left hand panel. (**b**) Equivalent analysis for a smaller, independent dataset (unconc2). (**c**) Equivalent analysis for a dataset obtained after concentrating virus through a sucrose cushion (conc). Only closed and weak classes were obtained. (**d-f**) Cut-open local resolution maps for structures shown in (a-c).

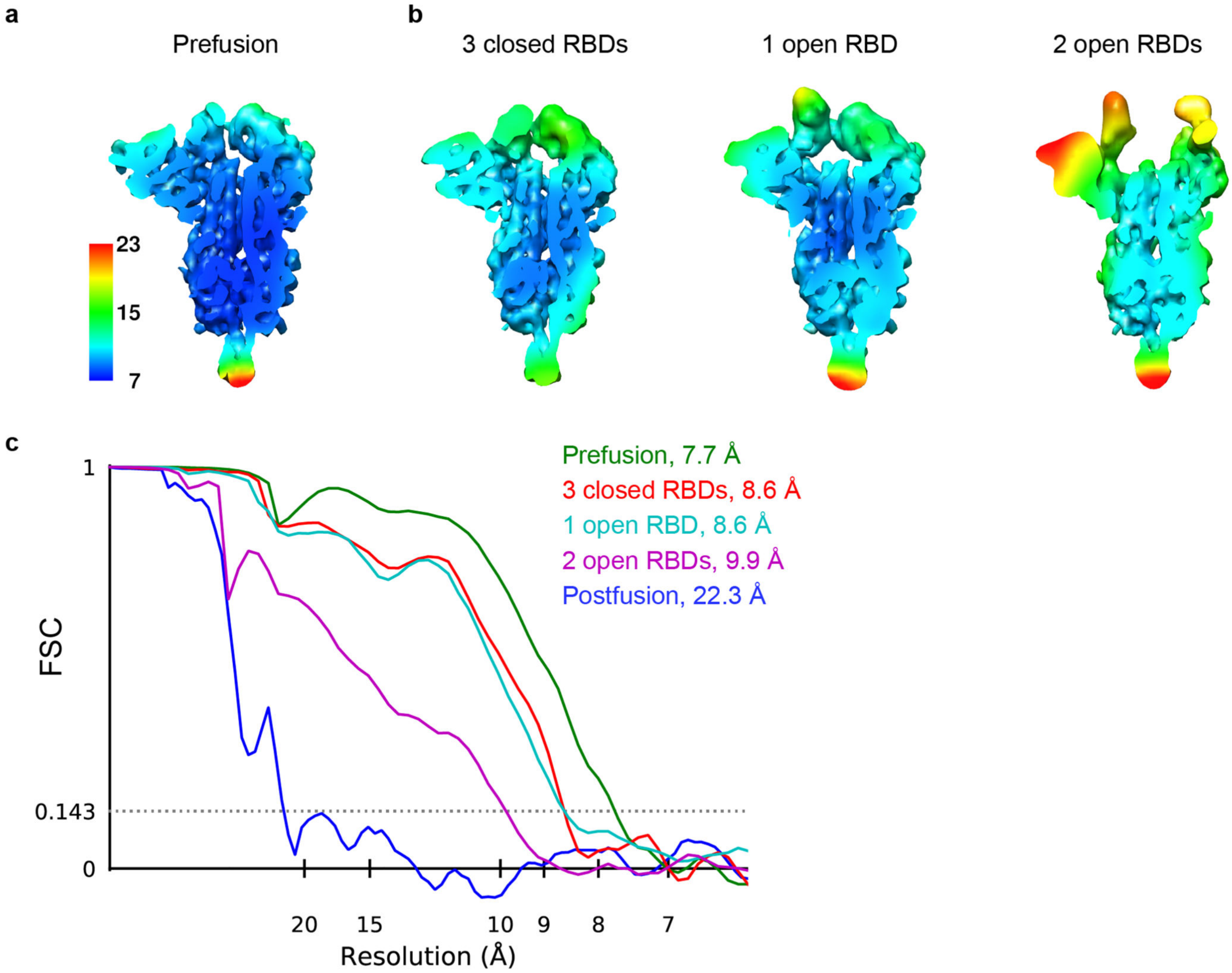

Extended Data Fig. 4. Resolution assessment of subtomogram averaging structures.

(**a**) Local resolution map for the consensus structure obtained for the prefusion S trimers. (**b**) Local resolution maps for the prefusion S trimer in three different conformations. (**c**) Global resolution assessment by Fourier shell correlation (FSC) at the 0.143 criterion for the four structures shown in a and b, as well as the postfusion S trimer.

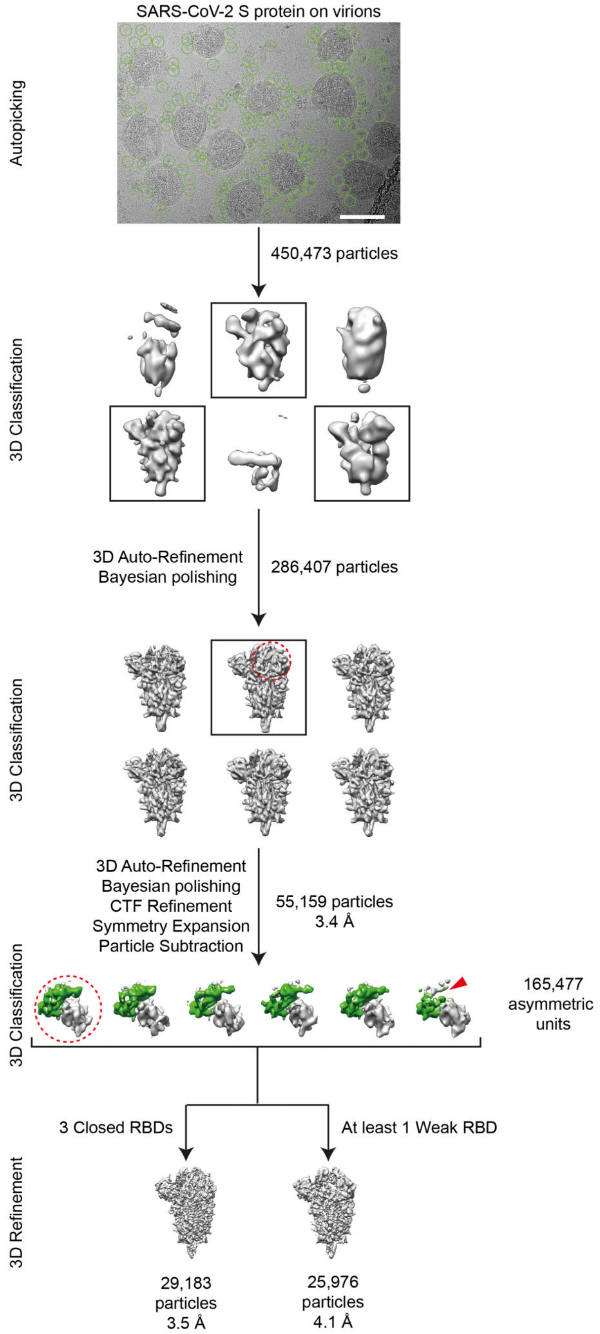

Extended Data Fig. 5. Single particle cryo-EM image processing workflow.

Automatically picked particles (green circles) were subjected to 3D classification. Scale bar 100 nm. Selected 3D classes are indicated by black boxes. RBDs from individual asymmetric units from the S trimer (red dashed circles) were locally classified to sort different conformations of RBD. The asymmetric unit subjected to local classification is shown in a top view, the RDB of the green monomer is weak in the right-hand class (red arrowhead). S trimers with all three RBDs in the closed state were further refined with C3 symmetry. S trimers where one RBD had weak density were refined with C1 symmetry. For further details see materials and methods.

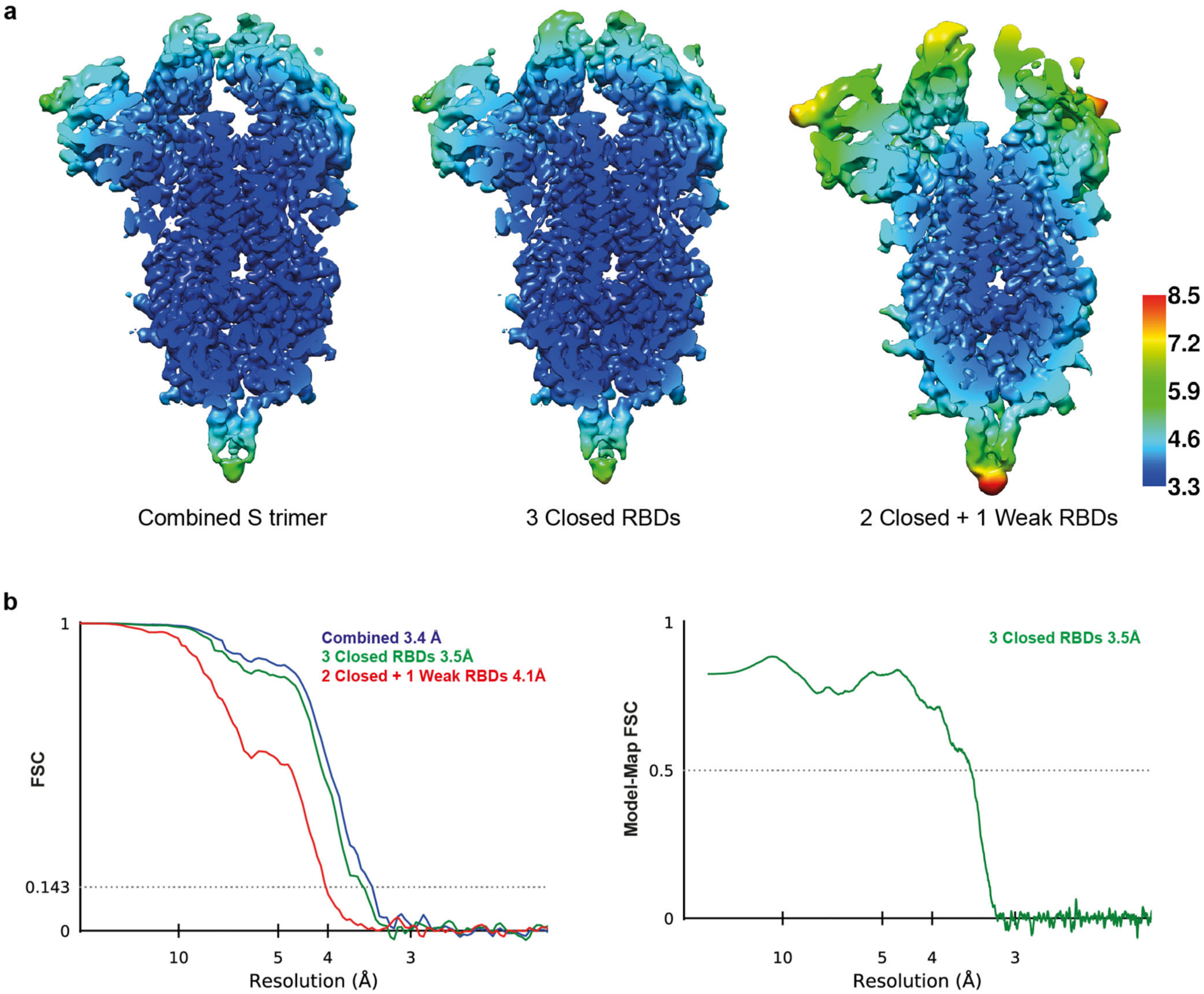

Extended Data Fig. 6. Single particle Cryo-EM structure validation.

(**a**) Cut-open cryo-EM maps obtained using all prefusion S trimers, S trimers with 3 closed RBDs or S trimers with 2 closed and 1 weak RBDs, coloured according to the local resolution. (**b**) FSC curves for the three structures in (a), and for the atomic model against the map.

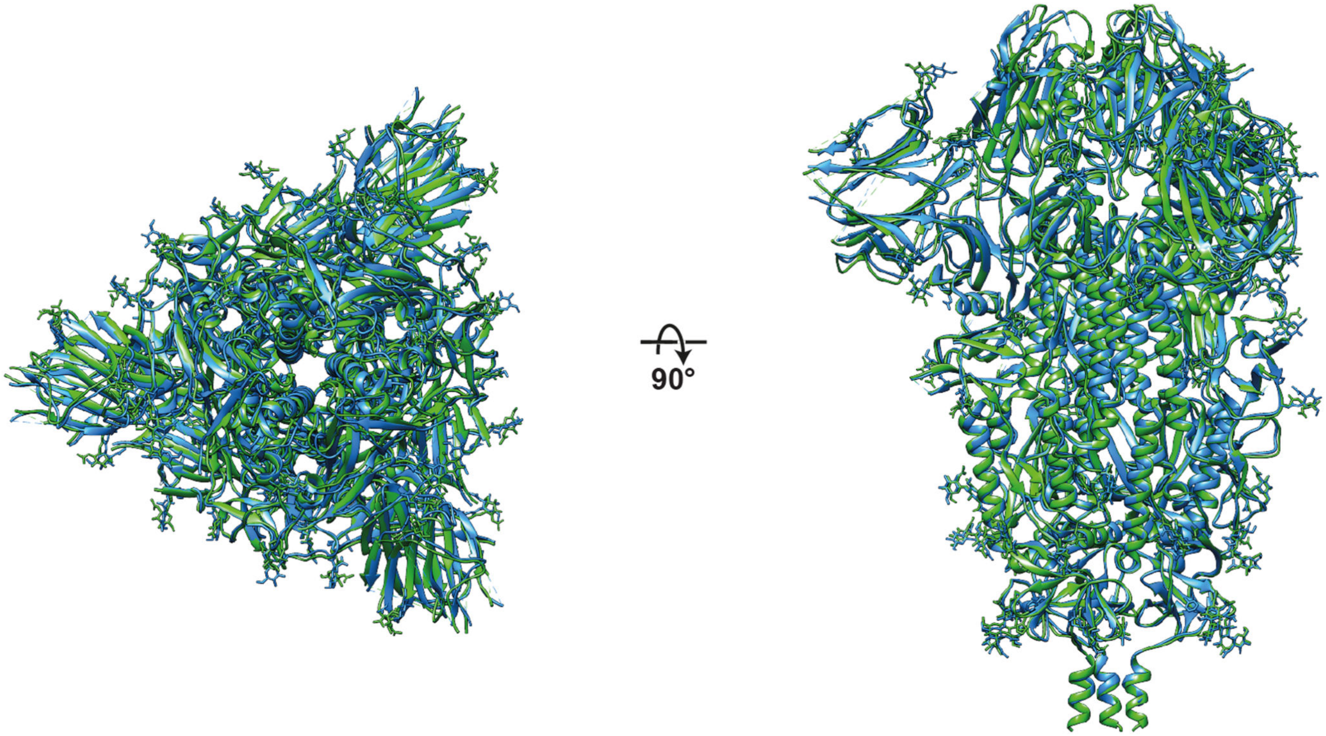

Extended Data Fig. 7. Structural comparison of *in situ* structure with recombinant soluble structure.

Structural superposition of S trimer modelled into the structure of the trimer with three closed RBDs (green, this study) with the published structure of recombinant, soluble closed trimer (blue, PDB 6VXX). Top and side views are shown. The structures are very similar.

Extended Data Table 1

Cryo-ET data acquisition and image processing

Sample	VeroE6 unconc 1	VeroE6 unconc 2	VeroE6 conc	Calu-3 unconc
Data Collection				
Microscope	FEI Titan Krios	FEI Titan Krios	FEI Titan Krios	FEI Titan Krios
Voltage (keV)	300	300	300	300
Energy-filter (eV)	20	20	20	20
Detector	Gatan K2 Summit	Gatan IC2 Summit	Gatan K2 Summit	Gatan K2 Summit
Recording Mode	Counting	Counting	Counting	Counting
Pixel size (Å)	1-532	1.532	1.532	1-532
Defocus range (pm)	-2 to-6	-2 to-6	-2 to -6	-2 to -6
Acquisition scheme	-60/60°, 3°	-60/60°, 3°	-60/60°, 3°	-60/60°, 3°
Total Dose (electrons/Å^2)	~120	~120	~120	~120
Frame number	10	10	10	10

Sample	VeroE6 unconc 1	VeroE6 unconc 2	VeroE6 conc	Calu-3 unconc
Tomograms	156	65	30	57
image processing				
Virus particles	179	68	227	NA
Subtomograms	4,104	1.335	4,136	NA
Symmetry	C3	C3	C3	NA
Resolution at 0.143 FSC(Å)	7.7	9.9	9.1	NA
EMDB ID	EMD-11493	*HA*	NA	
Spike trimer confotmation classification				

Trimer Classification	3 dosed RBDs	1 open RBD	2 open RBDs
Trimer partldes	U75	2,121	525
Symmetry	C3	C1	Cl
Resolution at 0.143 FSC (Å)	8.6	8.6	9.9
EMDB ID	EMD-11494	EMD-11495	EMD-11496

Extended Data Table 2

Cryo-EM data collection, refinement and validation statistics

	3 Closed RBDs (EMD-11497, PDB 6ZWV)	2 Closed + 1 Weak RBDs (EMD-11498)
Dala collection and processing		
Magnification	81,000	81,000
Voltage (kV)	300	300
Electron exposure (e-/Å^2)	50	50
Defocus range (μm)	1.0-3.0	1.0-3.0
Pixel size (Å)	1,061	1,061
Movies (no.)	7,982	7,982
Symmetry imposed	*C3*	*Cl*
Initial particle images (no.)	450,473	450,473
Final particle images (no.)	29,183	25,976
Map resolution (Å)	3.5	4.1
FSC threshold	0.143	0.143
Map resolution range (Å)	3.35-27.16	3.67-15.27
Refinement		
Initial model used	PDB 6ZP0	
Model resolution (Å)	3.5	
FSC threshold	0.5	
Map sharpening *B* factor (Å^2)	-50	
Model composition		
Non-hydrogen atoms	24036	

	3 Closed RBDs (EMD-11497, PDB 6ZWV)	2 Closed + 1 Weak RBDs (EMD-11498)
Protein residues	2955	
Ligands	63	
B factors (Å^2)		
Protein	130.57	
Ligand	142.74	
R.m.s. deviations		
Bond lengths (Å)	0.009	
Bond angles (°)	1.346	
Validation		
MolProbity score	1.62	
Clashscore	2.97	
Poor rotamers (%)	1.74	
Ramachandran plot		
Favored (%)	94.97	
Allowed (%)	5.03	
Disallowed (%)	0.00	

Supplementary Material

Refer to Web version on PubMed Central for supplementary material.

Acknowledgements

We thank the staff of the MRC-LMB for generous support during the COVID-19 pandemic lockdown. We thank all the staff of the MRC-LMB EM Facility, in particular Anna Yeates, Grigory Sharov and Giuseppe Cannone, for supporting the EM experiments and Jake Grimmett and Toby Darling for supporting scientific computing. We are grateful to C. Drosten and EVAg for provision of the SARS-CoV-2 strain used here, to Manfred Frey for the Calu-3 cell line, and we acknowledge microscopy support from the Infectious Diseases Imaging Platform (IDIP) at the Center for Integrative Infectious Disease Research Heidelberg. This study was supported by funding from the European Research Council (ERC) under the European Union's Horizon 2020 research and innovation programme (ERC-CoG-648432 MEMBRANEFUSION to JAGB), the Medical Research Council as part of United Kingdom Research and Innovation (MC_UP_A025_1013 to SHWS; MC_UP_1201/16 to JAGB), the Deutsche Forschungsgemeinschaft (240245660 – SFB 1129 project 5 to HGK and project 11 to RB) and the Japan Society for the Promotion of Science (overseas research fellowship to TN).

Data availability

Published structures for comparison or initial model building were obtained from the protein data bank (PDB) with accession codes 6VXX[2], 6VYB[2], 6X2B[11], 6XRA[8] and 6ZP0[9]. The cryo-EM and cryo-ET structures determined here, and representative tomograms are deposited in the Electron Microscopy Data Bank (EMDB) under accession codes EMD-11493 (prefusion consensus structure), EMD-11494 (3 closed RBDs from subtomogram averaging), EMD-11495 (1 open RBD), EMD-11496 (2 open RBDs), EMD-11497 (3 closed RBDs from cryo-EM), and EMD-11498 (2 open and 1 weak RBDs). The associated molecular models are deposited in the PDB under accession codes 6ZWV (3 closed RBDs from cryo-EM).

References

1. Neuman BW, Buchmeier MJ. Supramolecular Architecture of the Coronavirus Particle. Advances in Virus Research. 2016; 96:1–27. [PubMed: 27712621]
2. Walls AC, et al. Structure, Function, and Antigenicity of the SARS-CoV-2 Spike Glycoprotein. Cell. 2020; 181:281–292.e6. [PubMed: 32155444]
3. Hoffmann M, et al. SARS-CoV-2 Cell Entry Depends on ACE2 and TMPRSS2 and Is Blocked by a Clinically Proven Protease Inhibitor. Cell. 2020; 181:271–280.e8. [PubMed: 32142651]
4. Shang J, et al. Structural basis of receptor recognition by SARS-CoV-2. Nature. 2020; 581:221–224. [PubMed: 32225175]
5. Wang Q, et al. Structural and Functional Basis of SARS-CoV-2 Entry by Using Human ACE2. Cell. 2020; 181:894–904.e9. [PubMed: 32275855]
6. Watanabe Y, Allen JD, Wrapp D, McLellan JS, Crispin M. Site-specific glycan analysis of the SARS-CoV-2 spike. Science. 2020; doi: 10.1126/science.abb9983
7. Wrapp D, et al. Cryo-EM structure of the 2019-nCoV spike in the prefusion conformation. Science. 2020; 367:1260–1263. [PubMed: 32075877]
8. Cai Y, et al. Distinct conformational states of SARS-CoV-2 spike protein. Science. 2020; doi: 10.1126/science.abd4251
9. Xiong X, et al. A thermostable, closed SARS-CoV-2 spike protein trimer. Nat Struct Mol Biol. 2020; doi: 10.1038/s41594-020-0478-5
10. Toelzer C, et al. Unexpected free fatty acid binding pocket in the cryo-EM structure of SARS-CoV-2 spike protein. bioRxiv. 2020; doi: 10.1101/2020.06.18.158584
11. Henderson R, et al. Controlling the SARS-CoV-2 spike glycoprotein conformation. Nat Struct Mol Biol. 2020; doi: 10.1038/s41594-020-0479-4
12. McCallum M, Walls AC, Bowen JE, Corti D, Veesler D. Structure-guided covalent stabilization of coronavirus spike glycoprotein trimers in the closed conformation. Nat Struct Mol Biol. 2020; doi: 10.1038/s41594-020-0483-8
13. Zhu N, et al. A novel coronavirus from patients with pneumonia in China, 2019. N Engl J Med. 2020; 382:727–733. [PubMed: 31978945]
14. Zhou P, et al. A pneumonia outbreak associated with a new coronavirus of probable bat origin. Nature. 2020; 579:270–273. [PubMed: 32015507]
15. Masters, Ps; Perlman, S. Chapter 28 – CoronaviridaeFields Virology. 6th Edition. Vol. 1. Elsevier; 2013. 826–858.
16. Neuman BW, et al. Supramolecular Architecture of Severe Acute Respiratory Syndrome Coronavirus Revealed by Electron Cryomicroscopy. J Virol. 2006; 80:7918–7928. [PubMed: 16873249]
17. Bárcena M, et al. Cryo-electron tomography of mouse hepatitis virus: Insights into the structure of the coronavirion. Proc Natl Acad Sci U S A. 2009; 106:582–587. [PubMed: 19124777]
18. Walls AC, et al. Tectonic conformational changes of a coronavirus spike glycoprotein promote membrane fusion. Proc Natl Acad Sci U S A. 2017; 114:11157–11162. [PubMed: 29073020]
19. Yuan Y, et al. Cryo-EM structures of MERS-CoV and SARS-CoV spike glycoproteins reveal the dynamic receptor binding domains. Nat Commun. 2017; 8:15092. [PubMed: 28393837]
20. Fehr AR, Perlman S. Coronaviruses: An overview of their replication and pathogenesis. Methods Mol Biol. 2015; 1282:1–23. [PubMed: 25720466]
21. Klein S, et al. SARS-CoV-2 structure and replication characterized by in situ cryo-electron tomography. bioRxiv. 2020; doi: 10.1101/2020.06.23.167064
22. Snijder EJ, et al. A unifying structural and functional model of the coronavirus replication organelle: Tracking down RNA synthesis. PLOS Biol. 2020; doi: 10.1371/journal.pbio.3000715
23. Hoffmann M, Hofmann-Winkler H, Pöhlmann S. Priming time: How cellular proteases arm coronavirus spike proteins. Activation of Viruses by Host Proteases. 2018; doi: 10.1007/978-3-319-75474-1_4
24. Rothe C, et al. Transmission of 2019-NCOV infection from an asymptomatic contact in Germany. New England Journal of Medicine. 2020; 382:970–971.

25. Liu C, et al. Viral Architecture of SARS-CoV-2 with Post-Fusion Spike Revealed by Cryo-EM. bioRxiv. 2020; :1–17. DOI: 10.1101/2020.03.02.972927

26. Chlanda P, et al. The hemifusion structure induced by influenza virus haemagglutinin is determined by physical properties of the target membranes. Nat Microbiol. 2016:1–16050.

27. Xiong X, et al. Receptor binding by a ferret-transmissible H5 avian influenza virus. Nature. 2013; 497:392–396. [PubMed: 23615615]

28. Gui M, et al. Cryo-electron microscopy structures of the SARS-CoV spike glycoprotein reveal a prerequisite conformational state for receptor binding. Cell Res. 2017; 27:119–129. [PubMed: 28008928]

29. Bonnafous P, et al. Treatment of influenza virus with Beta-propiolactone alters viral membrane fusion. Biochim Biophys Acta - Biomembr. 2014; 1838:355–363.

30. Zhou T, et al. A pH-dependent switch mediates conformational masking of SARS-CoV-2 spike. bioRxiv. 2020; doi: 10.1101/2020.07.04.187989

31. Korber B, et al. Tracking changes in SARS-CoV-2 Spike: evidence that D614G increases infectivity of the COVID-19 virus. Cell. 2020; doi: 10.1016/j.cell.2020.06.043

32. Wan W, et al. Structure and assembly of the Ebola virus nucleocapsid. Nature. 2017; 551:394–397. [PubMed: 29144446]

33. Mastronarde DN. Automated electron microscope tomography using robust prediction of specimen movements. J Struct Biol. 2005; 152:36–51. [PubMed: 16182563]

34. Hagen WJH, Wan W, Briggs JAG. Implementation of a cryo-electron tomography tilt-scheme optimized for high resolution subtomogram averaging. J Struct Biol. 2017; 197:191–198. [PubMed: 27313000]

35. Kremer JR, Mastronarde DN, McIntosh JR. Computer visualization of three-dimensional image data using IMOD. J Struct Biol. 1996; 116:71–76. [PubMed: 8742726]

36. Grant T, Grigorieff N. Measuring the optimal exposure for single particle cryo-EM using a 2.6 Å reconstruction of rotavirus VP6. Elife. 2015; 4

37. Xiong Q, Morphew MK, Schwartz CL, Hoenger AH, Mastronarde DN. CTF determination and correction for low dose tomographic tilt series. J Struct Biol. 2009; 168:378–387. [PubMed: 19732834]

38. Turoňová B, Schur FKM, Wan W, Briggs JAG. Efficient 3D-CTF correction for cryo-electron tomography using NovaCTF improves subtomogram averaging resolution to 3.4 Å. J Struct Biol. 2017; 199:187–195. [PubMed: 28743638]

39. Galaz-Montoya JG, Flanagan J, Schmid MF, Ludtke SJ. Single particle tomography in EMAN2. J Struct Biol. 2015; 190:279–290. [PubMed: 25956334]

40. Nickell S, et al. TOM software toolbox: Acquisition and analysis for electron tomography. J Struct Biol. 2005; 149:227–234. [PubMed: 15721576]

41. Förster F, Medalia O, Zauberman N, Baumeister W, Fass D. Retrovirus envelope protein complex structure in situ studied by cryo-electron tomography. Proc Natl Acad Sci U S A. 2005; 102:4729–4734. [PubMed: 15774580]

42. Pettersen EF, et al. UCSF Chimera - A visualization system for exploratory research and analysis. J Comput Chem. 2004; 25:1605–1612. [PubMed: 15264254]

43. Qu K, et al. Structure and architecture of immature and mature murine leukemia virus capsids. Proc Natl Acad Sci U S A. 2018; 115:E11751–E11760. [PubMed: 30478053]

44. Bharat TAM, Russo CJ, Löwe J, Passmore LA, Scheres SHW. Advances in Single-Particle Electron Cryomicroscopy Structure Determination applied to Sub-tomogram Averaging. Structure. 2015; 23:1743–1753. [PubMed: 26256537]

45. Scheres SHW. Processing of Structurally Heterogeneous Cryo-EM Data in RELION. Methods Enzymol. 2016; 579:125–57. [PubMed: 27572726]

46. Zivanov J, et al. New tools for automated high-resolution cryo-EM structure determination in RELION-3. Elife. 2018; 7

47. Zheng SQ, et al. MotionCor2: anisotropic correction of beam-induced motion for improved cryo-electron microscopy. Nat Methods. 2017; 14:331–332. [PubMed: 28250466]

48. Rohou A, Grigorieff N. CTFFIND4: Fast and accurate defocus estimation from electron micrographs. J Struct Biol. 2015; 192:216–221. [PubMed: 26278980]

49. Bepler T, et al. Positive-unlabeled convolutional neural networks for particle picking in cryo-electron micrographs. Nat Methods. 2019; 16:1153–1160. [PubMed: 31591578]

50. Bai X, Rajendra E, Yang G, Shi Y, Scheres SHW. Sampling the conformational space of the catalytic subunit of human γ-secretase. Elife. 2015; 4

51. Emsley P, Cowtan K. Coot : model-building tools for molecular graphics. Acta Crystallogr Sect D Biol Crystallogr. 2004; 60:2126–2132. [PubMed: 15572765]

52. Kidmose RT, et al. Namdinator - Automatic molecular dynamics flexible fitting of structural models into cryo-EM and crystallography experimental maps. IUCrJ. 2019; doi: 10.1107/S2052252519007619

53. Afonine PV, et al. Real-space refinement in PHENIX for cryo-EM and crystallography. Acta Crystallogr Sect D Struct Biol. 2018; 74:531–544. [PubMed: 29872004]

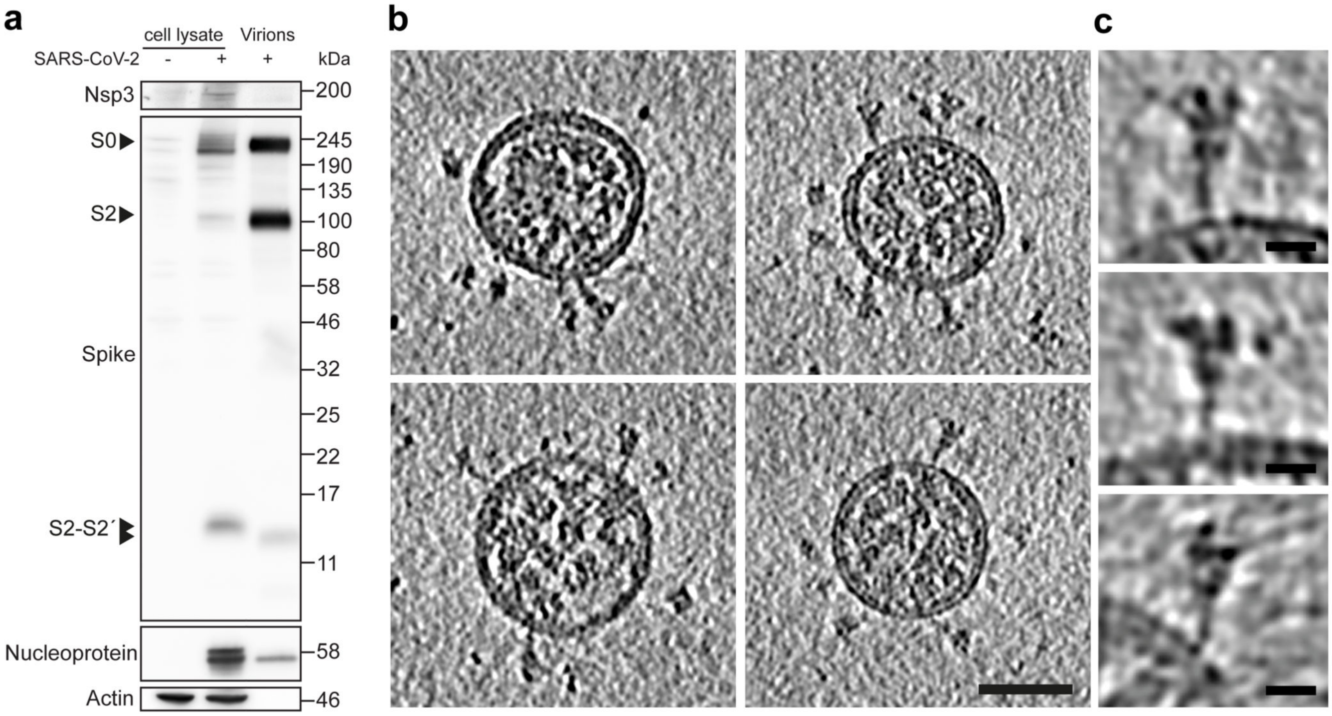

Fig .1. Characterization of virus production and images of SARS-CoV-2 virions.

(**a**) Western blot analysis of SARS-CoV-2 nsp3, S and N in lysates of VeroE6 cells and in virus preparations, representative of 3 experiments. In released virions, S is present in both cleaved and uncleaved forms. The positions of S0, S2 and the S2-S2’ cleavage product are marked. (**b**) Four representative tomographic slices of SARS-CoV-2 virions from the supernatant of infected cells. Virions are approximately spherical, contain granular density corresponding to N-packaged genome, and have S trimers protruding at variable angles from their surfaces. Scale bar 50 nm. (**c**) Three example S trimers from the dataset shown as projections through the trimer to illustrate variable tilt towards the membrane. Scale bar 10 nm.

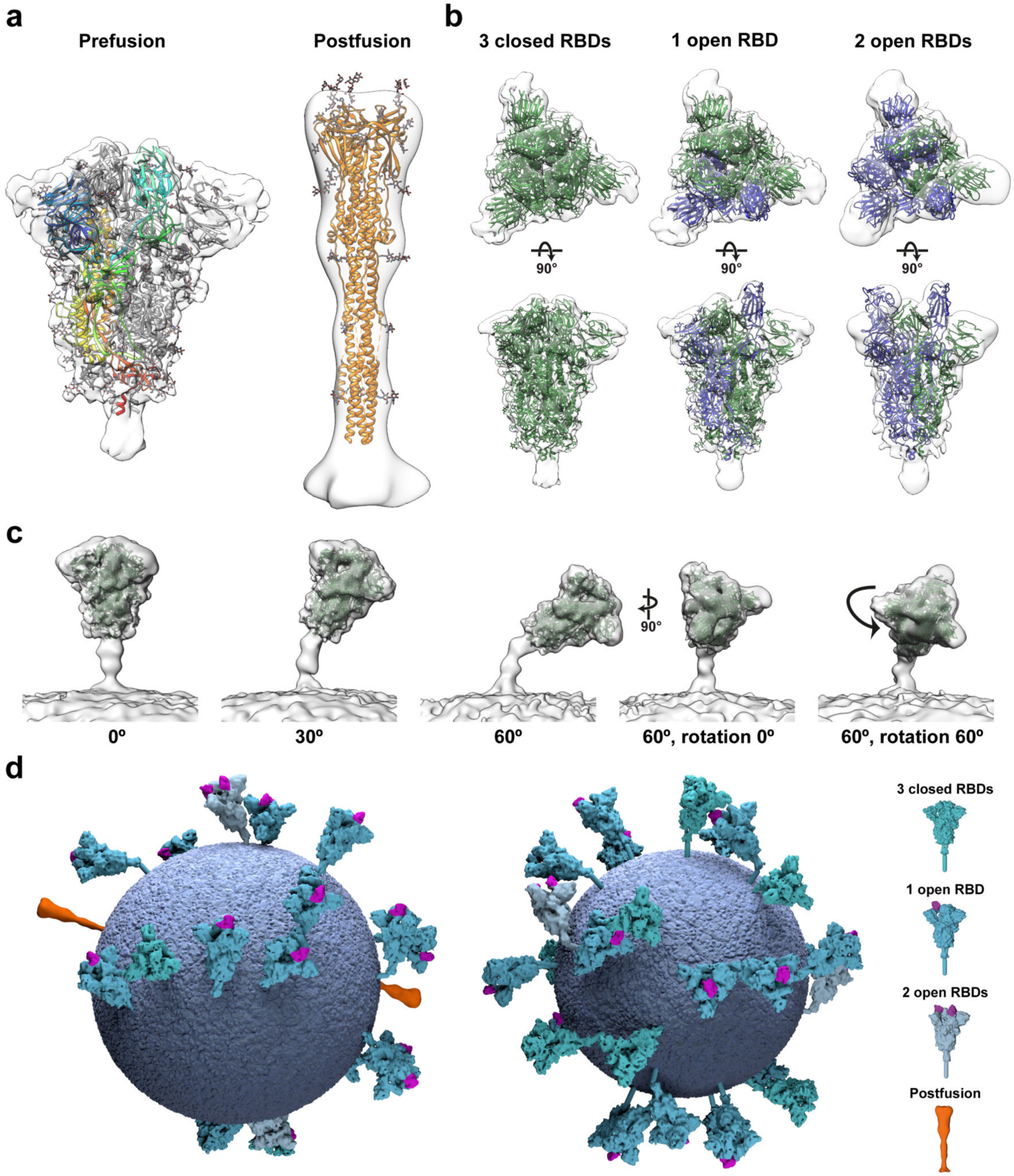

Fig. 2. Structural analysis of SARS-CoV-2 S trimers on intact virions.

(**a**) Structures of the prefusion (left) and postfusion (right) trimer from intact virions determined by subtomogram averaging. Structures are shown as transparent grey isosurfaces fitted with structures of the closed, prefusion trimer (PDB 6VXX) and the postfusion trimer (PDB 6XRA). One prefusion monomer is colored from blue (N terminus) to red (C terminus). The N-terminal domain is blue, the RBD appears cyan. The NTD does not fully occupy the EM density because some loops are not resolved or built in PDB 6VXX. (**b**) Three conformations of the prefusion trimer observed on intact virions: all RBDs in the closed position (left, fitted with PDB 6VXX); one RBD in the open position (center, fitted with PDB 6VYB); two RBDs in the open position (right, fitted with PDB 6X2B which lacks modelled glycans). The two-open conformation has only been observed *in vitro* after inserting multiple stabilizing mutations. S monomers with closed RBDs are green, and with open RBDs are blue. (**c**) Averaging of subsets of trimers grouped according to their orientation relative to the membrane shows flexibility in the stalk region. Examples are shown for pools centered at 0°, 30° and 60° from the perpendicular, and for two rotations of the trimer relative to the tilt direction. (**d**) 3D models of two individual SARS-CoV-2 virions with a membrane (blue) of the measured radius, and all spike proteins shown in the conformations, positions and orientations determined by subtomogram averaging. Different S conformations are distributed over the virion surface and can be tilted by up to ~90° relative to the membrane (Extended Data Fig. 1c,d).

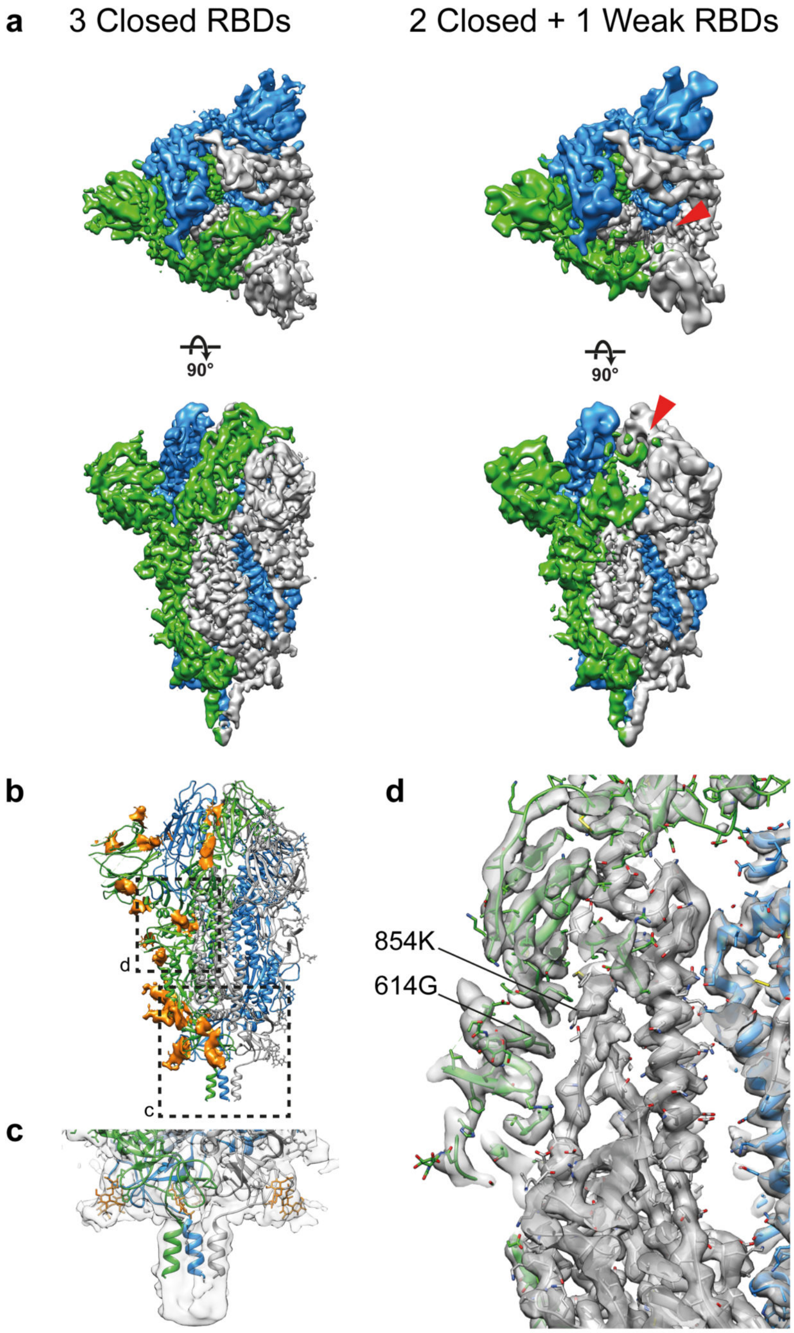

Fig. 3. Structures of SARS-CoV-2 S trimers on intact virions by single particle reconstruction.

(**a**) Top and side views of trimers with three closed RBDs (left, 3.5 Å resolution) and one weaker RBD (right, 4.1 Å resolution). Compare the left and right panels to see the weaker density for the RBD from the green monomer in the region indicated by the red arrowheads. Individual monomers are coloured white, blue and green. (**B**) Glycosylation profile of the S protein. Colour scheme as in (a), glycans are shown in orange. Boxes indicates the regions shown in c and d. (**c**) Close up of the base of the trimer at lower isosurface threshold to highlight the glycan ring and the extended C-terminal density. (**d**) Close up of the region of the spike where the D614G variation abolishes a salt bridge to 854K.